

Generalized non-exponential Gaussian splatting

SÉBASTIEN SPEIERER, Meta, Switzerland

ADRIAN JARABO, Meta, Spain

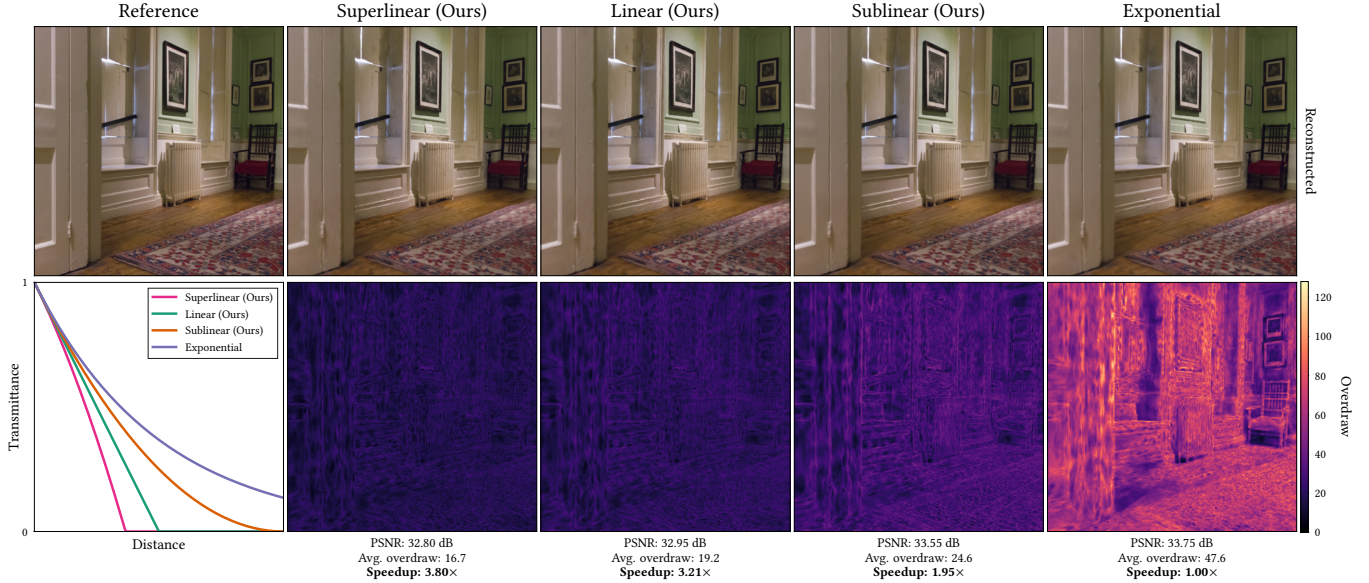


Fig. 1. **Non-exponential transmittance for 3D Gaussian Splatting (3DGS).** We compare the baseline exponential transmittance model implicit in 3DGS image formation model, against our new non-exponential transmittance models on the *Dr. Johnson* scene, refined from a pretrained 3DGS asset. *Top row:* Ground-truth reference (left) and reconstructed images for each transmittance model. *Bottom row:* A plot of the transmittance decay functions (left) and per-pixel overdraw count visualizations. Our non-exponential models achieve comparable image quality to the baseline model, while reducing overdraws by 3–4 \times , directly translating to faster rendering.

In this work we generalize 3D Gaussian splatting (3DGS) to a wider family of physically-based alpha-blending operators. 3DGS has become the standard de-facto for radiance field rendering and reconstruction, given its flexibility and efficiency. At its core, it is based on alpha-blending sorted semitransparent primitives, which in the limit converges to the classic radiative transfer function with exponential transmittance. Inspired by recent research on non-exponential radiative transfer, we generalize the image formation model of 3DGS to non-exponential regimes. Based on this generalization, we use a quadratic transmittance to define sub-linear, linear, and super-linear versions of 3DGS, which exhibit faster-than-exponential decay. We demonstrate that these new non-exponential variants achieve similar quality than the original 3DGS but significantly reduce the number of overdraws, which result on speed-ups of up to 4 \times in complex real-world captures, on a ray-tracing-based renderer.

CCS Concepts: • **Computing methodologies** \rightarrow **Rendering**.

Additional Key Words and Phrases: gaussian splatting, radiance fields, non-exponential transmittance

1 INTRODUCTION

Recent methods on radiance field rendering and reconstruction [Mildenhall et al. 2020] have allowed photorealistic rendering of real-world scenes and humans. In particular, *3D Gaussian splatting*

Authors’ addresses: Sébastien Speierer, speierers@meta.com, Meta, Switzerland; Adrian Jarabo, ajarabo@meta.com, Meta, Spain.

(3DGS) [Kerbl et al. 2023] has emerged as the most versatile representation, and its flexibility and efficiency have made it particularly attractive for applications including photorealistic avatars modeling [Qian et al. 2024; Saito et al. 2024], photorealistic rendering in virtual reality [Jiang et al. 2024], scene understanding [Jang and Kim 2025; Zhou et al. 2024a], or generative three-dimensional graphics [Tang et al. 2024].

3DGS uses trainable point-based volumetric semitransparent emissive primitives, whose contribution is accumulated in each pixel using multiplicative alpha-blending. While several alternatives over the building blocks of the original technique have been proposed, including alternative emissive functions [Diolatzis et al. 2024; Liu et al. 2025] or kernel primitives [Condor et al. 2025; Hamdi et al. 2024; Huang et al. 2025; Liu et al. 2025], the image formation model essentially stays the same.

In particular, the multiplicative-alpha-blending-based image formation model is a discrete form of, and in the limit converges to, the classic radiative transfer equation (RTE) [Chandrasekhar 2013; von Lommel 1889], which predicts an exponential transmittance under the assumption of volumes with uncorrelated particles. This contrast with nature and real-life matter, where correlation has been observed in most appearances, including clouds [Davis and Marshak 2004], vegetation [Knyazikhin et al. 1998], porous [Bellet

et al. 2009] and granular [Meng et al. 2015] materials, or periodic crystal-like structures [Caglioti and Golse 2003]. This has fostered the development of new radiative transfer frameworks [Bitterli et al. 2018; Jarabo et al. 2018], that generalized the classic RTE to non-exponential regimes.

In this work we generalize 3DGS to non-exponential transmittance regimes, by first relating it with the classic RTE, and then deriving its generalized non-exponential counterpart. Armed with this physically-based framework, we then derive a set of new 3DGS image formation models for the cases of linear- and quadratic-like transmittance functions, including its forward and differential modes using path-replay backpropagation [Vicini et al. 2021b]. We show that these faster-than-exponential transmittance modes allow to reconstruct photorealistic scenes with similar quality than the exponential model, with the additional benefit of significantly less overdraws, which translates into speed-ups of up-to around 4× in real-world scenes in our ray-tracing-based renderer compared to the baseline exponential model, as exemplified in Fig. 1.

2 RELATED WORK

3D Gaussian splatting. A vast literature exists using and extending 3D Gaussian splatting: From the original proposal of Kerbl et al. [2023], several works have been published improving on certain aspects of the method, including new kernels beyond Gaussians [Condor et al. 2025; Hamdi et al. 2024; Huang et al. 2025; Liu et al. 2025], new directional emission functions replacing spherical harmonics [Diolatzis et al. 2024; Liu et al. 2025], spatially-varying textured emission [Xu et al. 2024], or alternative primitives including linear primitives [von Lützwow and Nießner 2025], 3D convexes [Held et al. 2025c], triangles [Held et al. 2025b] and meshes [Held et al. 2025a]. Other works have focused on increasing the problem dimensionality to the temporal domain [Wu et al. 2024; Yang et al. 2023], improving the robustness of the optimization process [Kulhanek et al. 2024; Rota Bulò et al. 2024; Sabour et al. 2025; Yin et al. 2025], or providing scalable solutions for large scenes [Feng et al. 2025; Ren et al. 2025]. All these works are based on the same exponential image formation model; our work is orthogonal to these efforts, proposing a generalized image formation model based on novel alpha-blending compositing techniques of the splats.

Non-exponential light transport. Non-exponential or generalized transport have been studied in fields including radiative transfer, optics and neutron transport (see [d’Eon 2022] for an in-depth discussion). In graphics, the first work exploring non-exponential regimes was the work by Moon et al. [2007] in the context of granular media, from a phenomenological approach. A more formal definition of the problem was introduced by d’Eon [2014], though practical rendering of non-exponential media was not possible until the works of Jarabo et al. [2018] and Bitterli et al. [2018], which explored the problem from two alternative perspectives: Jarabo et al. analyzed the problem from a purely radiative perspective, while Bitterli et al. developed a path-integral-based framework. Both works proposed different non-exponential transmittance functions based on the statistical properties of the media, similar to the one used by Wrenninge et al. [2017]; this model was later extended by Guo et al. [2019] introducing a more general transmittance model based on

fractional Gaussian fields. Vicini et al. [2021a] exploited the additional representation power of non-exponential media to improve reconstruction of volumetric assets, which was also used by Condor and Jarabo [2022] to accelerate rendering of complex luminaries. Closer to us, Zhou et al. [2024b] used a linear transmittance model for closed-form integration of volumetric 3D Gaussians for physics-based rendering. In contrast, our work leverages non-exponential light transport for defining new alpha-blending operators in the context of infinitesimal splats.

Alpha blending and transparency. From the initial work of Smith and Catmull [Smith 1995] on alpha compositing, alpha blending has been a fundamental tool in graphics. Porter and Duff’s [1984] seminal work established the mathematical foundation for compositing digital images. Blinn [2002a,b] provided new derivations of the over operator and implementation considerations for various pixel formats. Glassner [2015] revisited the interpretation of alpha, providing a consistent and physically meaningful model of pixel structure, which we use as foundation for our model. Further works have generalized and formalized alpha compositing: Willis [2006] proposed a projective alpha color model, which unifies various compositing approaches using an algebraic perspective, while Duff [2017] analyzed deep compositing using Lie algebras, providing a rigorous mathematical framework for advanced compositing operations. Our work can be seen as a generalization of the alpha blending operator defined by an arbitrary asymptotic transmittance of semitransparent layers.

3 GAUSSIAN SPLATTING

3D Gaussian splatting [Kerbl et al. 2023] uses a set of ellipsoidal volumetric semi-transparent primitives (*Gaussians*)¹ to model the radiance emitted in a scene. Each primitive is represented by its directional emission $E_i(\omega)$, center c_i , covariance Σ_i , and opacity \mathfrak{N}_i . The contribution of each primitive to a pixel is defined by a kernel $K(\mathbf{x}|\{\mathbf{x}_i, \Sigma_i\})$ (usually a Gaussian, but others exist), which we use to compute the pixel opacity $\alpha_i(\mathbf{y}) = \mathfrak{N}_i \cdot K(\mathbf{y}|\{\mathbf{x}_i, \Sigma_i\})$.

Then, for a point \mathbf{x} in space (e.g., a sensor’s pixel), the incident radiance $L(\mathbf{x}, \omega)$ from direction ω is computed as the sum of emitted radiance by a set of N volumetric primitives projected to \mathbf{x} from direction ω as,

$$L_0(\mathbf{x}, \omega) = \sum_{i=1}^N E_i(\omega) \cdot \alpha_i(\mathbf{x}_i) \cdot \prod_{j<i} (1 - \alpha_j(\mathbf{x}_j)) + L_b(\mathbf{x}_b, \omega) \cdot \prod_{i=1}^N (1 - \alpha_i(\mathbf{x}_i)), \quad (1)$$

with $\mathbf{x}_i = \mathbf{x} - \omega \cdot t_i$, t_i the distance of the primitive i to \mathbf{x} , and L_b the contribution from the background. The first summand is the contribution of the Gaussians, and the second is the contribution from the background due to transparency; this second term is generally omitted, but we include it here for completeness. In the following, we remove it for simplicity. This formulation assumes that Gaussians are projected as billboards oriented towards the camera (*splats*), which is the common image formation model in Gaussian

¹For consistency with the related literature, during the text we will use the term *Gaussian* to name the primitives, though the kernel used might be different.

splatting. Note that while other works have proposed working with truly-volumetric primitives [Celarek et al. 2025; Condor et al. 2025; Kheradmand et al. 2025], in this work we focus on the splat-based image formation model. The splats are sorted front-to-bottom, so that $\forall i < j$ then $t_i < t_j$. In the following, we remove the spatial and directional dependency for clarity.

Physical interpretation. The image formation model in Equation (1) is a multiplicative alpha-blending. In this context, we can interpret α_i as the area coverage of occluding matter normalized by the unit volume [Porter and Duff 1984]. This has the physical unit of m^{-1} , and describes the probability of being occluded in the differential thickness of the splat, analogous to what in linear transport is the *differential probability of extinction* [d’Eon 2022].

It is trivial to see that Equation (1) is the discrete counterpart of the radiative transfer equation (RTE) [Chandrasekhar 2013] for emissive volumes, so that is equivalent to write (see proof in Section A)

$$L_0 = \int_0^\infty Q(\mathbf{x}_t) \cdot \sigma(\mathbf{x}_t) \cdot \overbrace{e^{-\tau_t}}^{T(\tau_t)} dt, \quad (2)$$

with $\mathbf{x}_t = \mathbf{x} - \boldsymbol{\omega} \cdot t$ with t the length along the ray, $\tau_t = \int_0^t \sigma(\mathbf{x}_s) ds$ the optical depth, $T(\tau_t)$ the exponential transmittance predicted by the Beer-Boulder-Lambert law, and $\sigma(\mathbf{x}_s)$ and $Q(\mathbf{x}_s)$ the density and emission fields, respectively derived from the splats along the ray as

$$\sigma(\mathbf{x}_t) = \sum_{i=1}^N \delta(t - t_i) \alpha_i \quad \text{and} \quad Q(\mathbf{x}_t) = \sum_{i=1}^N \delta(t - t_i) E_i, \quad (3)$$

with δ the Dirac delta.

Going deeper on the physical foundations of this model, a key assumption leading us to an exponential-like behavior in Eq. (2) is that the probability of extinction at each splat is an independent statistical process (see [Kostinski 2001, 2002]). For this to happen, the underlying coverage at each differential point in a splat needs to be fully uncorrelated from all the other splats contributing to a pixel. Intuitively, we can think of a splat as a disk formed by infinitesimally small random particles uniformly distributed in 2D, occluding light with probability equal to its density α_i . Assuming two uncorrelated splats occluding 50% of the light each, occlusion at each splat will be an statistically-independent process, so the total unoccluded light after passing through the two splats will be $(1 - 0.5) \times (1 - 0.5) = 0.25$ (Fig. 2, a). However, if the particles in the second splat are fully negatively correlated to the particles from the first one, all light that passes through the first one will hit particles in the second one, and the total light passing through the two splats will be $1 - 0.5 - 0.5 = 0$, forming a waterproof surface occluding all light (Fig. 2, b).

4 NON-EXPONENTIAL SPLATTING

In this section, we generalize the image formation model of 3DGS to arbitrary transmittance regimes. For that, we exploit the relationship between continuous and discrete media, and leverage the generalization of the RTE to non-exponential regimes to derive our new non-exponential splatting method. Then, we propose and evaluate a new set of non-exponential image formation models.

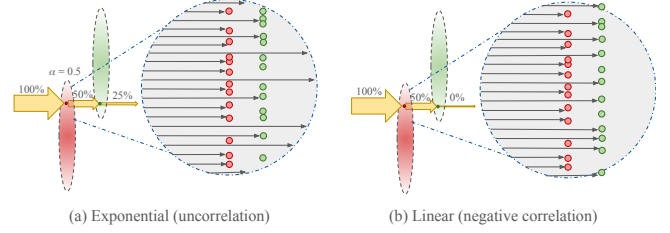


Fig. 2. **Physical interpretation of splats.** Splats can be thought as disk consisting of small random occluding particles. When light passes through an slab, some light is lost when hitting these particles. For uncorrelated splats (a), light occlusion in each splat is an independent stochastic process. For negatively-correlated splats (b), on the other hand, all light that passes through the first slab is occluded by the second one.

4.1 Background: The generalized Boltzmann equation

To account for regimes where light transport does not exhibit exponential transmittance, Larsen [2007] proposed the generalized Boltzmann equation (GBE), which in its integral form for emissive media reads

$$L_0 = \int_0^\infty Q(\mathbf{x}_t) \cdot \sigma(\mathbf{x}_t, \tau_t) \cdot T(\tau_t) dt. \quad (4)$$

For emissive media, the GBE is almost identical to the classic RTE with a key difference: The differential extinction probability $\sigma(\mathbf{x}_t, \tau_t)$ is not constant, but depends on the distance traveled by photons before being extinguished. This has a major implication in the rest of the terms governing the light transport, since $\sigma(\mathbf{x}_t, \tau_t)$, the path-length distribution² $p(\tau_t)$, and the transmittance $T(\tau_t)$ are directly related by

$$\sigma(\mathbf{x}_t, \tau_t) = \frac{p(\tau_t)}{T(\tau_t)}, \quad \text{with} \quad p(\tau_t) = -\frac{d}{dt} T(\tau_t) = -\sigma(\mathbf{x}_t) \cdot \frac{d}{d\tau} T(\tau_t). \quad (5)$$

Note that since we are modeling a non-scattering medium Larsen’s GBE holds in our case; if we would be also considering scattering we would need to account for a more complex form to maintain reciprocity [Bitterli et al. 2018; d’Eon 2018; Jarabo et al. 2018].

4.2 Our method

Equipped with Eqs. (4) and (5) we can just simplify the GBE as the product of the path-length distribution and emission, following:

$$L_0 = \int_0^\infty Q(\mathbf{x}_t) \cdot p(\tau_t) dt, \quad (6)$$

which by using the relationship between continuous and discrete media described in Eq. (3), we can just write the contribution of each Gaussian as a function of their emission and their probability of extinction. Including back the background contribution, the

²The path-length distribution, also known as probability of extinction or chord-length distribution, is the probability of being extinguished after traveling certain optical depth. Do not confuse it with the *differential* extinction probability $\sigma(\mathbf{x}_t, t)$, which is the probability of extinction when traveling a differential step.

Table 1. Summary of the mother transmittance functions $T(\tau_t)$ and the corresponding discrete probabilities $\bar{p}_{i < k}$ for $i < k$ used in our experiments. The *linear* transmittance was proposed by Jarabo et al. [2018] to stochastically model negatively-correlated opaque surfaces. The *quadratic* is an empirical transmittance, that generalizes the linear transmittance providing sublinear and superlinear decays. The *blended* transmittance reformulates the blended transmittance proposed by Vicini et al. [2021a], which is a linear combination of linear and exponential transmittance. Finally, the *power-law* model was proposed by Davis and Marshak [2004] to model fractal fluctuations in positively-correlated media. The operator $[x]_+ = \max(x, 0)$ is the clamping operator.

Name	Parameters	$T(\tau_t)$	$\bar{p}_{i < k}$
Exponential	N/A	$\exp(-\tau_t)$	$\alpha_i \cdot \prod_{j < i} (1 - \alpha_j)$
Linear	N/A	$[1 - \tau_t]_+$	α_i
Quadratic	$c \in [-0.5, \infty)$	$[1 - \tau_t - \frac{c}{2} \cdot \tau_t^2]_+$	$\alpha_i \cdot (1 + c \cdot \bar{\tau}_i)$
Blended	$\gamma \in [0, 1]$	$[\text{lerp}(1 - \tau_t, \exp(-\tau_t), \gamma)]_+$	$\alpha_i \cdot (1 - \gamma + \gamma \cdot \prod_{j < i} (1 - \alpha_j))$
[Vicini et al. 2021a]	$\gamma \in [0, 1]$	$\text{lerp}([1 - \tau_t]_+, \exp(-\tau_t), \gamma)$	$\text{lerp}(\bar{p}_{i < k}^{\text{lin}}, \bar{p}_{i < k}^{\text{exp}}, \gamma)$
Power-Law	$v \in (-1, \infty]$	$[(1 + \tau_t \cdot v)^{-1/v}]_+$	$\alpha_i \cdot (1 + \tau_i \cdot v)^{-\frac{1+\gamma}{v}}$

generalized Gaussian splatting image formation model becomes

$$L_0 = \underbrace{\sum_{i=1}^N E_i \cdot \bar{p}_i}_{\text{Splats}} + \underbrace{L_b \cdot \bar{T}_{N+1}}_{\text{Background}}, \quad (7)$$

where \bar{p}_i is the discrete probability of extinction for Gaussian i which depends on the *mother* transmittance function $T(\tau_t)$ chosen for defining the model, and with $\bar{T}_i = 1 - \sum_{j < i} \bar{p}_j$ the discrete transmittance operator.

This equation is general, and works with any arbitrary base transmittance function as soon it is physically correct. We detail later how to choose such base transmittance functions, but a key aspect that needs to be considered is that it always needs to be in greater or equal to zero. With that constraint, we can just define the discrete probability of extinction of each Gaussian as

$$\bar{p}_i = \begin{cases} -\frac{d}{dt} T(\bar{\tau}_i) & i < k, \\ 1 - \sum_{j < k} \bar{p}_j & i = k, \\ 0 & \text{otherwise,} \end{cases} \quad (8)$$

with $\bar{\tau}_i = \sum_{j < i} \alpha_j$ the discrete optical depth, and k the primitive that saturates transmittance so that $\sum_{i=0}^k p_i \geq 1$ and $\sum_{i=0}^{k-1} p_i < 1$. Note that allowing for a primitive to saturate transmittance is a key benefit from the generalized image formation model: Given the multiplicative nature of the original Gaussian splatting, transmittance never saturates to zero, and thus it is impossible to create fully-opaque appearances except for splats with $\alpha_i = 1$. In contrast, in our model this fully-opaque behavior can be easily achieved by choosing the appropriate base transmittance function.

4.3 Choosing a transmittance function

Our image formation model allows to use any arbitrary base transmittance function $T(\tau_t)$ to define the blending of the different splats. However, for the transmittance to be physically meaningful there are two conditions that must be taken into account: Given the physical definition of transmittance $T(\tau_t) = 1 - \int_0^t p(\tau_s) ds$, and since the path-length distribution $p(\tau_t)$ is a probability distribution, then a) transmittance is always in the interval $T(\tau_t) \in [0, 1]$ with $T(0) = 1$, and b) it is always non-increasing. In addition to these two physical constraints, c) we impose that the slope of the transmittance function at $\tau_t = 0$ is $p(0) = \frac{d}{dt} T(0) = \frac{d}{dt} \tau_t = \sigma(0)$, which effectively

makes the contribution of the first splat being always its opacity $p_1 = \alpha_1$. Thus, the transmittance function only plays a role when blending several splats.

With these three constraints, we propose six transmittance functions, listed in Table 1, for which we analyze their performance in toy-examples. Later in the radiance field experiments (Section 5) we focus on the *linear* and *quadratic* mother transmittance functions.

4.4 Evaluation

Transmittance. We first evaluate the emerging transmittance when blending a large set of low-opacity Gaussians. This allows us to validate that the discrete transmittance $\bar{T}_i = 1 - \sum_{j < i} p_j$ converges to the mother continuous transmittance function $T(\tau_t)$. Figure 3 shows the results for transmittance functions with increasing effective decay rate. As the effective decay rate increases, the appearance gets more opaque, with transmittance quickly saturating to zero. This results in significantly less overdraws for dense areas.

Blending. Figure 4 shows the results of blending three colored Gaussians using different mother transmittance functions $T(\tau_t)$, in two scenarios. In both cases, the results are similar, showing sharper blending of the back Gaussians when using faster-than-exponential transmittance functions, while at the same time obtaining more opaque appearances, as shown in the inverse transmittance images.

5 RESULTS

We evaluate our non-exponential transmittance models in two experimental settings: (i) *reconstruction from scratch*, where a 3D Gaussian Splatting (3DGS) representation is optimized from COLMAP point clouds and multi-view images, and (ii) *refinement of existing assets*, where a pre-trained 3DGS scene produced by a conventional rasterization-based renderer is fine-tuned under our ray-tracing pipeline. In both cases, we compare three proposed transmittance decay functions — superlinear, linear, and sublinear — against the baseline exponential transmittance in the original 3DGS formulation [Kerbl et al. 2023]. The two non-linear transmittance functions are implemented using the quadratic transmittance with $c = -0.5$ (sublinear) and $c = 0.5$ (superlinear) respectively.

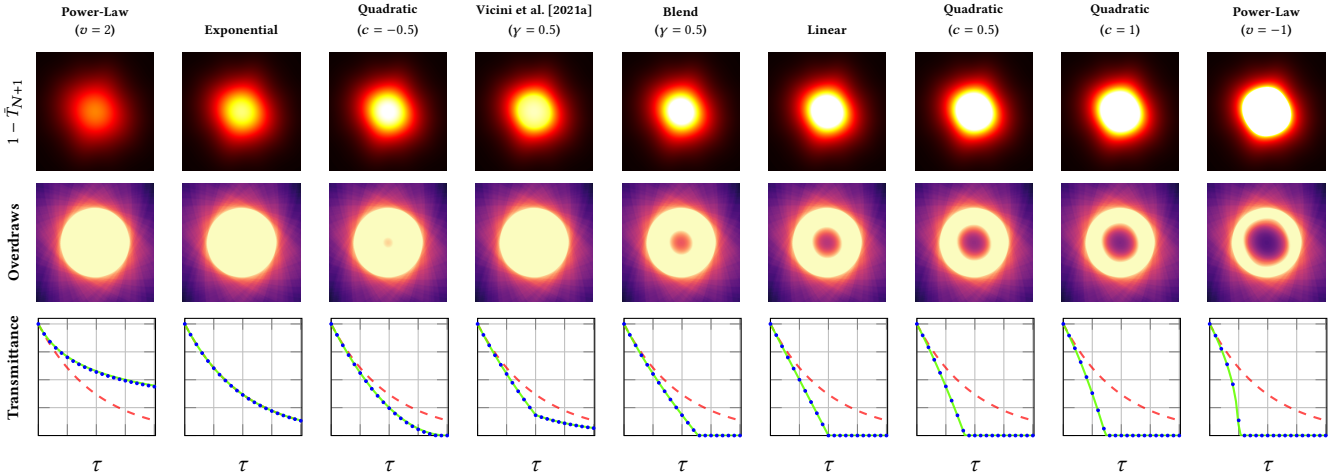


Fig. 3. **Transmittance comparison.** We render 100 elliptical Gaussians with random rotation with opacity $\mathfrak{N} = 0.02$, distributed uniformly in depth, for nine different transmittance functions, and compute the inverse transmittance $1 - \bar{T}_{N+1}$ per pixel (top) and the number of overdraws until transmittance saturates (middle, colormap goes from black to yellow). The bottom plots show the theoretical mother transmittance $T(\tau_t)$ of each model (green) compared with the baseline exponential (dashed red), and the discrete transmittance \bar{T}_i at the rendered splats (blue dots). Our predicted discrete transmittance matches the theoretical one, which validates that our generalized model for splatting converges to the continuous generalized RTE. The faster is the decay, the less overdraws are required to saturate, and the more opaque is the reconstructed appearance.

5.1 Implementation Details

Renderer. Our pipeline is implemented on top of Mitsuba [Jakob et al. 2022]. Unlike the tile-based rasterizer of Kerbl et al. [2023], our renderer evaluates Gaussian primitives via ray tracing, following the approach of Moenne-Loccoz et al. [2024]. For each pixel, a ray is cast through the scene’s bounding volume hierarchy and collects all intersected Gaussians. Each intersected Gaussian i is rendered as a billboard at a single depth t_i , located at the peak location of the Gaussian along the ray. The intersected Gaussians are composited front-to-back, with early termination when the accumulated transmittance \bar{T}_i saturates to zero. The maximum number of Gaussians along the ray is set to $N = 128$ and all experiments were conducted on a single NVIDIA RTX A6000 GPU.

For fairness, all results computed using the baseline exponential transmittance are computed through our same pipeline and renderer. Since ray-tracing is usually slower than rasterization-based pipelines, the provided numbers with the baseline are slower than previous works’. However, they serve as a baseline reference in terms of both quality and speed-ups.

Loss function. Similar to Kerbl et al. [2023] we use a image-space loss in sRGB space combining the ℓ_1 and the structural similarity (SSIM) losses, following

$$\mathcal{L} = (1 - \lambda) \mathcal{L}_1 + \lambda \mathcal{L}_{\text{SSIM}}. \quad (9)$$

Optimization. We use the bounded Adam optimizer [Conder et al. 2025] with per-parameter learning rates modulated by an exponential decay schedule from an initial rate of 1.0 down to 0.1 (see Table 2 for all hyperparameters used in the optimization). For the backward phase, we use path-replay backpropagation [Vicini et al. 2021b], with the recursive adjoints derived in Section C.

Coarse-to-fine scheduling. We use a coarse-to-fine strategy to accelerate convergence at early steps. Training starts at $\frac{1}{4}$ resolution and is upsampled to $\frac{1}{2}$ resolution at iteration 64, then to full resolution at iteration 200. The refinement pipeline operates at full resolution throughout, since the Gaussians are already well-initialized from the pretrained model.

Adaptive density control. We adopt the densification strategy of Kerbl et al. [2023]. Every 100 iterations, Gaussians with accumulated positional gradient magnitude exceeding 5×10^{-6} are candidates for splitting. We split along the longest axis and disable cloning, as we found split-only densification to be more stable for our transmittance models. Pruning is applied every 200 iterations, removing Gaussians with opacity below 0.008 or maximum scale below 10^{-4} . Densification is active only during the first 3,000 iterations, and the maximum primitive count is capped at 200,000. In the refinement pipeline, both densification and pruning are *disabled*; the Gaussian count is inherited from the pretrained model (~ 3.4 M primitives for realistic scenes).

5.2 Reconstruction

Initialization. Gaussians are initialized from a sparse points obtained using COLMAP [Schönberger and Frahm 2016], with scales set to each point’s nearest-neighbor distance (clamped to maximum scale of 0.02), identity quaternion rotations, and initial opacity of 0.1. Colors are initialized from the COLMAP point colors. We additionally scatter 15,000 random Gaussians to help filling unobserved regions.

Training budget. To highlight the practical impact of rendering speed on optimization throughput, we impose a *wall-clock time budget* rather than a fixed iteration count. For reconstruction, each

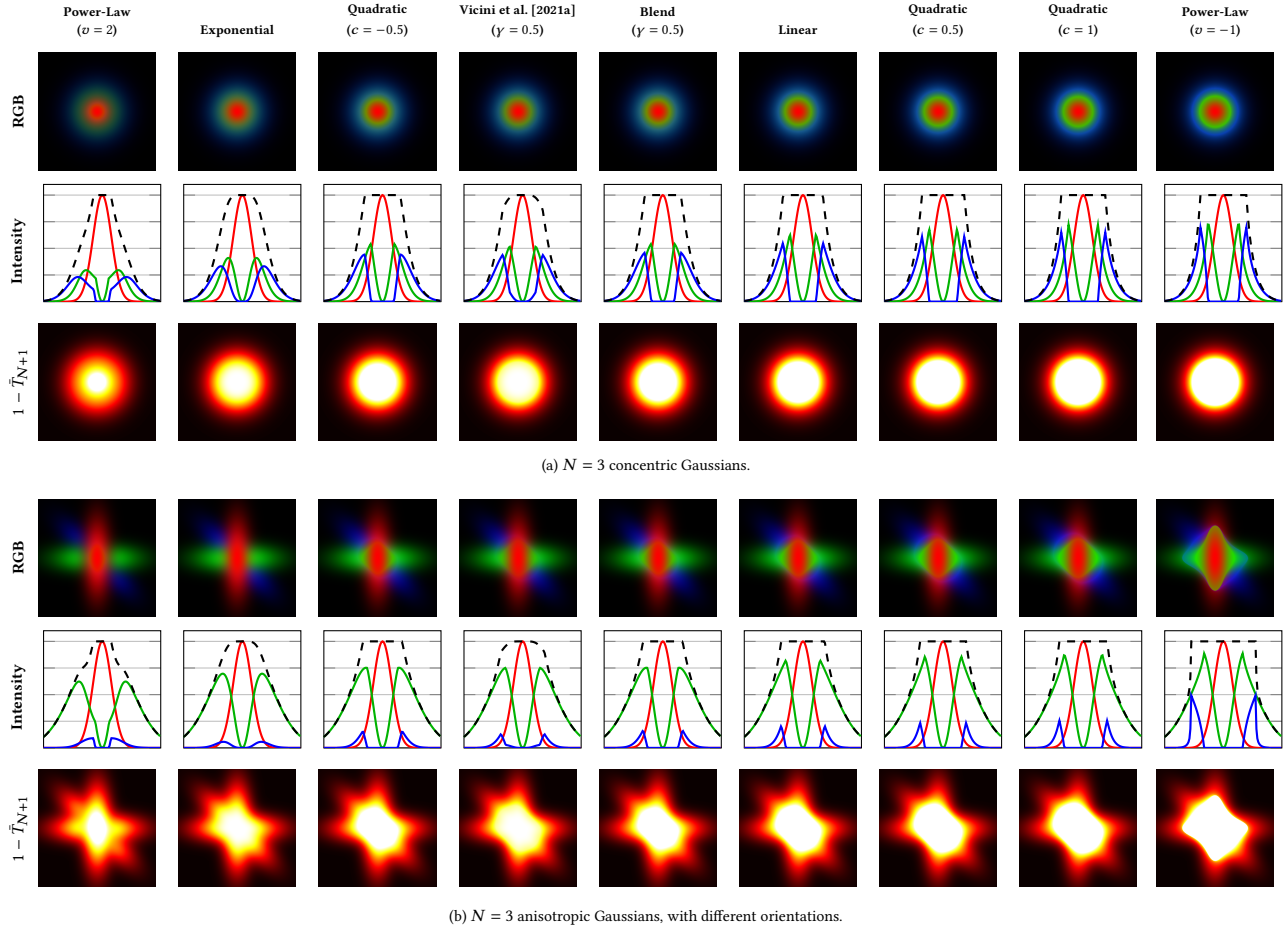


Fig. 4. **Blending comparison.** We render 3 Gaussians with different colors and depths (red is closer, then green, and blue at the back) with opacity $\aleph = 1$, and (a) without anisotropy and growing in size and (b) anisotropic and with different rotations in the image plane. All splats are parallel to the image plane, and do not intersect. In both (a) and (b), the top row shows the result of blending, the middle row shows the scan-line at the center of the top image (with the black dashed line the sum of the three Gaussians), and the bottom row is the inverse discrete transmittance $1 - \bar{T}_{N+1}$. Faster-than-exponential transmittance (third to ninth columns) show sharper blending, which for extreme cases (power-law with $v = -1$) results in unintuitive blending: This sharper blending behavior is in part due to transparency saturating to one (see middle row), which creates C_1 discontinuities on the blended primitives. Only the exponential transmittance does not show this behavior, due to the statistical uncorrelation between each splat, at the cost of more overdraws.

run is limited to 5,000 s (~ 83 min) with a maximum of 15,000 iterations. Within this budget, the superlinear model completes roughly 13,000 iterations, while the exponential baseline manages only $\sim 3,300$ —a $\sim 4\times$ difference in optimizer steps, directly attributable to the lower per-iteration rendering cost.

Results. We evaluate reconstruction quality on four scenes from the NeRF synthetic dataset [Mildenhall et al. 2020] (*Chair, Hotdog, Lego, Materials*). Quality and performance metrics are summarized in the top half of Tables 3 and 4, respectively, and a visual comparison is shown in Fig. 5.

As reported in Table 3, the superlinear model achieves the highest average PSNR (30.13 dB) and SSIM (0.9705), and the lowest MSE (0.0010), outperforming the exponential baseline (28.99 dB, SSIM 0.9547, MSE 0.0014) by over 1 dB on average. The linear model follows closely (29.88 dB, SSIM 0.9677), while even the sublinear

variant matches the exponential baseline in PSNR while producing substantially less overdraw. This quality advantage is a direct consequence of the reduced rendering and optimization cost: as shown in Table 4, the superlinear model renders at 50.3 FPS on average compared to 9.1 FPS for the exponential model—a $5.5\times$ speedup—with an average overdraw of only 16.2 (72.1 for the baseline). Under a fixed 5,000 s training budget, this speed-up allows the optimizer to complete $\sim 4\times$ more steps, leading to a substantially better-converged reconstruction.

Figure 5 provides a qualitative comparison. Each scene is shown as a row, with the ground-truth reference on the left and the four transmittance models to the right. The rightmost column shows PSNR convergence over both wall-clock time and iterations: the non-exponential models converge faster in wall-clock time due to their lower per-iteration cost, while their per-iteration convergence

rate remains comparable to the exponential baseline. PSNR and FPS values are annotated below each image.

5.3 Refinement

Initialization. We start from a pre-trained 3DGS asset, obtained through the implementation of Kerbl et al. [2023] with the standard image formation model, including the parameters of the Gaussians, their opacity and SH color coefficients.

Training budget. For refinement, the budget is 1,800 s (30 min) with a maximum of 1,000 iterations; the faster methods comfortably finish all iterations, while the exponential baseline may not.

Results. For the refinement experiment, we use two indoor scenes (*Dr Johnson* and *Playroom* [Barron et al. 2022]), and two outdoor scenes (*Train* and *Truck* [Knapitsch et al. 2017]). We start from pretrained models using the original splatting-based renderer [Kerbl et al. 2023] (30,000 iterations, exponential transmittance). We fine-tune these assets using our ray-tracing pipeline, continuing the optimization for up to 1,000 iterations (or 30 min). Densification and pruning are disabled; only the existing Gaussian parameters are fine-tuned. Tables 3 and 4 (bottom half) show the reconstruction quality and performance metrics for each scene, while Fig. 6 presents a qualitative comparison.

The quality metrics in Table 3 confirm that our non-exponential models maintain image fidelity after refinement. The sublinear model achieves the best average PSNR (25.90 dB) and SSIM (0.8407), closely followed by the exponential baseline (25.85 dB, SSIM 0.8399). The linear and superlinear variants are less than 1 dB worse on average, demonstrating that the Gaussians originally trained under exponential transmittance can be successfully adapted to non-exponential models with minimal quality loss.

The performance gains remain substantial even in this refinement setting (Table 4). The superlinear model achieves 18.9 FPS on average versus 4.8 FPS for the exponential baseline—a 3.9× speedup—while reducing average overdraw from 47.9 to 15.7. Figure 6 shows that the refined images are visually similar across methods, while the overdraw insets clearly reveal the efficiency advantage of the non-exponential models.

6 DISCUSSION

We have seen experimentally that our faster-than-exponential transmittance models consistently achieve 3–5× rendering speed-ups with small-to-negligible impact on image quality, even improving quality in the reconstruction case by enabling more optimization iterations within the same time budget. The quadratic superlinear model offers the best trade-off between speed and quality: It consistently delivers the highest FPS and lowest overdraw while remaining highly competitive in terms of image quality. The linear model provides a balanced middle ground, while the sublinear variant sacrifices some speed for the closest quality match to the exponential baseline—making it the safest drop-in replacement while still resulting in a significant speed-up.

Limitations and Future Work. One limitation of our work is that we have only experimented our transmittance models with ray-tracing, which limits the comparison with state-of-the-art Gaussian

Table 2. Hyperparameters used for the reconstruction and refinement experiments.

Parameter	Recon.	Refine.
Max iterations	15 000	1 000
Wall-clock budget	5 000 s	1 800 s
Max primitives	200 000	(inherited)
Centers LR	0.13	0.015
Scales LR	0.08	0.03
Quaternions LR	0.45	0.1
Opacity LR	1.0	1.0
SH coefficients LR	2.0	0.2
LR schedule	Exp. decay	Exp. decay
SSIM weight λ	0.2	0.2
Coarse-to-fine	4× → 2× → 1×	Disabled
Densification interval	100 it.	Disabled
Pruning interval	200 it.	Disabled
SH degree	1	(inherited)

splatters. However, our new non-exponential models can be directly ported to rasterization, which would still benefit from the significant reduction in overdraws using faster-than-exponential transmittance models, though sorting would still be required. Note however that this performance gain is only possible if early termination when transmittance saturates is available.

More conceptually, order-independent stochastic transparency techniques [Kheradmand et al. 2025] are only available for exponential transmittance, where the binary Russian roulette applied on the splats differential extinction probability is independent from previous splats. See Section B for a more thorough explanation. This is a similar problem to delta tracking in heterogeneous non-exponential media [Bitterli et al. 2018], and requires further investigation.

Finally, we have assumed a fixed pre-defined transmittance during optimization. Including the transmittance parameters in the optimization, even adaptively per Gaussian following the approach of Vicini et al. [2021a], might increase the reconstruction quality, by giving additional degrees of freedom in the image formation model.

Relationship with alpha blending. Our image formation model defined by Eqs. (7) and (8) offers a physically-grounded form for deriving new alpha blending operators, with any arbitrary decay function. This directly relates with the physical interpretation provided by Glassner [2015] of alpha and compositing, and in particular on how blending two semitransparent layers would depend on the correlation between these two layers. For example, as described in Fig. 2, the linear attenuation is a form of perfectly negative correlation between scatterers. Further exploring physically-based transmittance functions capable to model the whole range of inter-matter correlation (from negative to positive) is still an open problem.

Conclusion. We have generalized 3D Gaussian splatting to support non-exponential transmittance regimes. From a theoretical point of view, this has helped to link 3DGS with continuous volume rendering. From the family of non-exponential 3DGS models we have proposed, we have explored the usability of the quadratic transmittance, analyzing the performance of superlinear, linear and sublinear decays on radiance field reconstruction. Our results

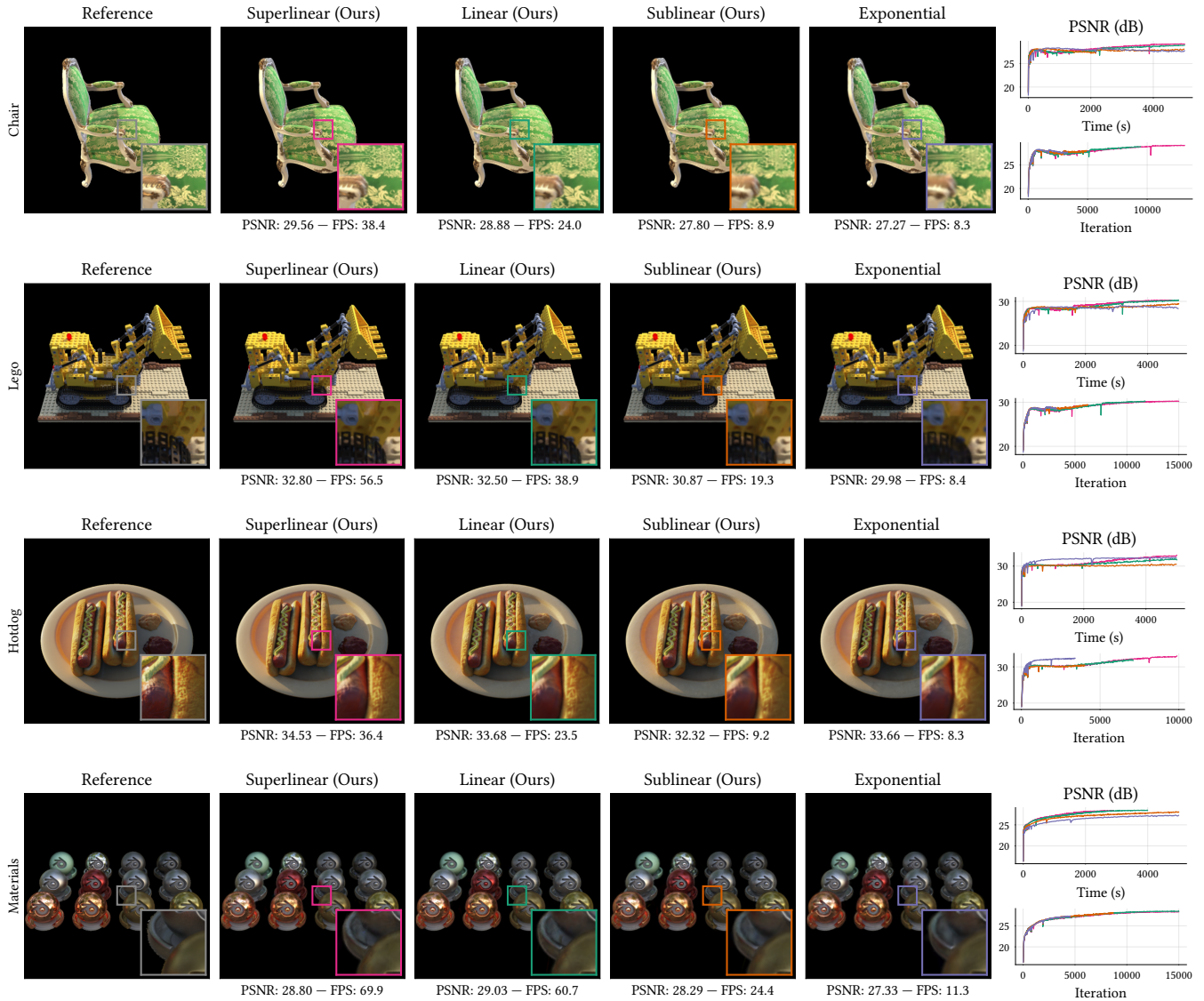


Fig. 5. **Reconstruction results on NeRF synthetic scenes.** Each row shows one scene (*Chair*, *Hotdog*, *Lego* and *Materials*), with the ground-truth reference on the left and the reconstructions using each of the four image formation models to the right. The rightmost column plots PSNR convergence over wall-clock time (top) and iteration count (bottom). Under a fixed time budget, the non-exponential models run significantly more iterations and converge to a higher PSNR, while per-iteration convergence remains comparable across all models.

show that these new 3DGS models achieve comparable quality to their classic exponential counterpart, while achieving 3 – 4× less overdraws, directly translated on significant speed-up during rendering and training.

REFERENCES

- Jonathan T. Barron, Ben Mildenhall, Dor Verbin, Pratul P. Srinivasan, and Peter Hedman. 2022. Mip-NeRF 360: Unbounded Anti-Aliased Neural Radiance Fields. In *Proceedings of CVPR*.
- Fabien Bellet, Elie Chalopin, Florian Fichot, Estelle Iacona, and Jean Taine. 2009. RDFI determination of anisotropic and scattering dependent radiative conductivity tensors in porous media: Application to rod bundles. *International Journal of Heat and Mass Transfer* 52, 5-6 (2009), 1544–1551.
- Benedikt Bitterli, Srinath Ravichandran, Thomas Müller, Magnus Wrenninge, Jan Novák, Steve Marschner, and Wojciech Jarosz. 2018. A radiative transfer framework for non-exponential media. *ACM Trans. Graph.* 37, 6 (2018), 1–17.
- James F. Blinn. 2002a. Compositing. 1. Theory. *IEEE Computer Graphics and Applications* 22, 1 (2002), 83–87. doi:10.1109/38.974522
- James F. Blinn. 2002b. Compositing, Part 2: Practice. *IEEE Computer Graphics and Applications* 22, 2 (2002), 78–82. doi:10.1109/38.988747
- Emanuele Caglioti and François Golse. 2003. On the distribution of free path lengths for the periodic Lorentz gas III. *Communications in Mathematical Physics* 236, 2 (2003), 199–221.
- Adam Celarek, George Kopanas, George Drettakis, Michael Wimmer, and Bernhard Kerbl. 2025. Does 3D Gaussian Splatting Need Accurate Volumetric Rendering? *Computer Graphics Forum* (2025), e70032.



Fig. 6. **Refinement results on real scenes.** Each row shows one scene (*Dr Johnson*, *Playroom*, *Train* and *Truck*), with the ground-truth reference on the left and the reconstructions using each of the four image formation models to the right. Insets show the per-pixel overdrawing count. The non-exponential models maintain comparable visual quality comparable to the exponential baseline while substantially reducing overdraw, which results into 3–4× rendering speedups.

Table 3. Image quality metrics across reconstruction and refinement experiments.

Scene	Superlinear (Ours)			Linear (Ours)			Sublinear (Ours)			Exponential		
	PSNR↑	MSE↓	SSIM↑	PSNR↑	MSE↓	SSIM↑	PSNR↑	MSE↓	SSIM↑	PSNR↑	MSE↓	SSIM↑
<i>Reconstruction</i>												
Chair	29.16	0.0012	0.9721	28.85	0.0013	0.9654	28.13	0.0015	0.9530	27.72	0.0017	0.9471
Hotdog	32.77	0.0005	0.9777	32.01	0.0006	0.9735	30.52	0.0009	0.9669	32.39	0.0006	0.9731
Lego	30.26	0.0009	0.9748	30.19	0.0010	0.9731	29.44	0.0011	0.9622	28.61	0.0014	0.9536
Materials	28.33	0.0015	0.9573	28.47	0.0014	0.9589	28.04	0.0016	0.9532	27.26	0.0019	0.9448
<i>Average</i>	30.13	0.0010	0.9705	29.88	0.0011	0.9677	29.03	0.0013	0.9588	28.99	0.0014	0.9547
<i>Refinement</i>												
Drjohnson	31.64	0.0007	0.9490	31.70	0.0007	0.9496	32.59	0.0006	0.9578	32.37	0.0006	0.9574
Playroom	30.20	0.0010	0.9096	30.27	0.0009	0.9109	30.45	0.0009	0.9152	30.71	0.0008	0.9195
Train	16.77	0.0210	0.6332	17.19	0.0191	0.6433	18.01	0.0158	0.6839	17.75	0.0168	0.6741
Truck	21.98	0.0063	0.7778	22.08	0.0062	0.7829	22.53	0.0056	0.8062	22.58	0.0055	0.8087
<i>Average</i>	25.15	0.0073	0.8174	25.31	0.0067	0.8217	25.90	0.0057	0.8407	25.85	0.0059	0.8399

Table 4. Rendering performance across reconstruction and refinement experiments.

Scene	Superlinear (Ours)			Linear (Ours)			Sublinear (Ours)			Exponential		
	FPS↑	Speedup↑	Avg. OD↓	FPS↑	Speedup↑	Avg. OD↓	FPS↑	Speedup↑	Avg. OD↓	FPS↑	Speedup↑	Avg. OD↓
<i>Reconstruction</i>												
Chair	38.4	4.63×	17.8	24.0	2.89×	20.8	8.9	1.07×	34.2	8.3	1.00×	79.0
Hotdog	36.4	4.39×	18.7	23.5	2.83×	21.0	9.2	1.11×	35.4	8.3	1.00×	73.2
Lego	56.5	6.73×	13.9	38.9	4.63×	18.2	19.3	2.30×	28.0	8.4	1.00×	70.3
Materials	69.9	6.19×	14.6	60.7	5.37×	16.8	24.4	2.16×	26.6	11.3	1.00×	65.9
<i>Average</i>	50.3	5.49×	16.2	36.8	3.93×	19.2	15.5	1.66×	31.0	9.1	1.00×	72.1
<i>Refinement</i>												
Drjohnson	10.3	3.81×	16.7	8.7	3.22×	19.2	5.3	1.96×	24.6	2.7	1.00×	47.6
Playroom	11.3	3.90×	15.8	9.7	3.34×	18.1	6.4	2.21×	21.1	2.9	1.00×	50.3
Train	30.5	4.18×	15.3	26.7	3.66×	17.7	15.9	2.18×	24.1	7.3	1.00×	48.6
Truck	23.7	3.65×	14.9	20.6	3.17×	17.0	13.2	2.03×	21.7	6.5	1.00×	45.0
<i>Average</i>	18.9	3.89×	15.7	16.4	3.35×	18.0	10.2	2.09×	22.9	4.8	1.00×	47.9

Jorge Condor, Sébastien Speierer, Lukas Bode, Aljaz Bozic, Simon Green, Piotr Didyk, and Adrian Jarabo. 2025. Don't Splat your Gaussians: Volumetric Ray-Traced Primitives for Modeling and Rendering Scattering and Emissive Media. *ACM Trans. Graph.* 44, 1 (2025), 1–17.

Anthony B. Davis and Alexander Marshak. 2004. Photon propagation in heterogeneous optical media with spatial correlations: enhanced mean-free-paths and wider-than-exponential free-path distributions. *Journal of Quantitative Spectroscopy and Radiative Transfer* 84, 1 (2004), 3–34.

Stavros Diolatzis, Tobias Zirr, Alexander Kuznetsov, Georgios Kopanas, and Anton Kaplanyan. 2024. N-dimensional Gaussians for fitting of high dimensional functions. In *Proceedings of SIGGRAPH Conference Papers*. 1–11.

Tom Duff. 2017. Deep Compositing Using Lie Algebras. *ACM Trans. Graph.* 36, 3 (2017), 1–13. doi:10.1145/3023386

Eugene d'Eon. 2014. Computer graphics and particle transport: our common heritage, recent cross-field parallels and the future of our rendering equation. In *Digipro 2014*.

Eugene d'Eon. 2018. A reciprocal formulation of nonexponential radiative transfer. 1: Sketch and motivation. *Journal of Computational and Theoretical Transport* 47, 1-3 (2018), 84–115.

Eugene d'Eon. 2022. A Hitchhiker's Guide to Multiple Scattering. <http://www.eugenedeon.com/hitchhikers>. Accessed: 2026-01-21.

Eric Enderton, Erik Sintorn, Peter Shirley, and David Luebke. 2010. Stochastic transparency. In *Proceedings of the I3D*. 157–164.

Guofeng Feng, Siyan Chen, Rong Fu, Zimu Liao, Yi Wang, Tao Liu, Boni Hu, et al. 2025. FlashGS: Efficient 3D Gaussian Splatting for Large-Scale and High-Resolution Rendering. In *Proceedings of CVPR*. 26652–26662.

Andrew S. Glassner. 2015. Interpreting Alpha. *Journal of Computer Graphics Techniques* 4, 2 (2015), 30–44. <https://www.jcgt.org/published/0004/02/03/paper-lowres.pdf>

Jie Guo, Yanjun Chen, Bingyang Hu, Ling-Qi Yan, Yanwen Guo, and Yuntao Liu. 2019. Fractional Gaussian Fields for Modeling and Rendering of Spatially-Correlated Media. *ACM Trans. Graph.* 38, 4 (2019).

Abdullah Hamdi, Luke Melas-Kyriazi, Jinjie Mai, Guocheng Qian, Ruoshi Liu, Carl Vondrick, Bernard Ghanem, and Andrea Vedaldi. 2024. Ges: Generalized exponential splatting for efficient radiance field rendering. In *Proceedings of CVPR*. 19812–19822.

Jan Held, Sanghyun Son, Renaud Vandeghen, Daniel Rebain, Matheus Gadelha, Yi Zhou, Anthony Cioppa, Ming C. Lin, Marc Van Droogenbroeck, and Andrea Tagliasacchi. 2025a. MeshSplatting: Differentiable Rendering with Opaque Meshes. *arXiv preprint arXiv:2512.06818* (2025).

Jan Held, Renaud Vandeghen, Adrien Deliege, Abdullah Hamdi, Silvio Giancola, Anthony Cioppa, Andrea Vedaldi, Bernard Ghanem, Andrea Tagliasacchi, and Marc Van Droogenbroeck. 2025b. Triangle Splatting for Real-Time Radiance Field Rendering. *arXiv preprint arXiv:2505.19175* (2025).

Jan Held, Renaud Vandeghen, Abdullah Hamdi, Adrien Deliege, Anthony Cioppa, Silvio Giancola, Andrea Vedaldi, Bernard Ghanem, and Marc Van Droogenbroeck. 2025c. 3D Convex Splatting: Radiance Field Rendering with 3D Smooth Convexes. In *Proceedings of CVPR*. 21360–21369.

Yi-Hua Huang, Ming-Xian Lin, Yang-Tian Sun, Ziyi Yang, Xiaoyang Lyu, Yan-Pei Cao, and Xiaojuan Qi. 2025. Deformable Radial Kernel Splatting. In *Proceedings of CVPR*. 21513–21523.

Wenzel Jakob, Sébastien Speierer, Nicolas Roussel, Merlin Nimier-David, Delio Vicini, Tizian Zeltner, Baptiste Nicolet, Miguel Crespo, Vincent Leroy, and Ziyi Zhang. 2022.

Mitsuba 3 renderer. <https://mitsuba-renderer.org>.

SungMin Jang and Wonjun Kim. 2025. Identity-aware language Gaussian splatting for open-vocabulary 3D semantic segmentation. In *Proceedings of ICCV*. 20467–20476.

Adrian Jarabo, Carlos Aliaga, and Diego Gutierrez. 2018. A radiative transfer framework for spatially-correlated materials. *ACM Trans. Graph.* 37, 4 (2018), 1–13.

Ying Jiang, Chang Yu, Tianyi Xie, Xuan Li, Yutao Feng, Huamin Wang, Minchen Li, Henry Lau, Feng Gao, Yin Yang, and Chenfanfu Jiang. 2024. VR-GS: A Physical Dynamics-Aware Interactive Gaussian Splatting System in Virtual Reality. In *Proceedings of SIGGRAPH Conference Papers*.

Bernhard Kerbl, Georgios Kopanas, Thomas Leimkühler, and George Drettakis. 2023. 3D Gaussian splatting for real-time radiance field rendering. *ACM Trans. Graph.* 42, 4 (2023), 139–1.

Shakiba Kheradmand, Delio Vicini, George Kopanas, Dmitry Lagun, Kwang Moo Yi, Mark Matthews, and Andrea Tagliasacchi. 2025. StochasticSplats: Stochastic Rasterization for Sorting-Free 3D Gaussian Splatting. *arXiv preprint arXiv:2503.24366* (2025).

Arno Knapitsch, Jaesik Park, Qian-Yi Zhou, and Vladlen Koltun. 2017. Tanks and Temples: Benchmarking Large-Scale Scene Reconstruction. *ACM Trans. Graph.* 36, 4 (2017).

Yuri Knyazikhin, Jörn Kranigk, Ranga B. Myneni, Oleg Panforyorov, and Gode Gravenhorst. 1998. Influence of small-scale structure on radiative transfer and photosynthesis in vegetation canopies. *Journal of Geophysical Research: Atmospheres* 103, D6 (1998), 6133–6144.

Alexander B Kostinski. 2001. On the extinction of radiation by a homogeneous but spatially correlated random medium. *Journal of the Optical Society of America A* 18, 8 (2001), 1929–1933.

Alexander B Kostinski. 2002. On the extinction of radiation by a homogeneous but spatially correlated random medium: reply to comment. *Journal of the Optical Society of America A* 19, 12 (2002), 2521–2525.

Jonas Kulhanek, Songyou Peng, Zuzana Kukelova, Marc Pollefeys, and Torsten Sattler. 2024. WildGaussians: 3D Gaussian Splatting in the Wild. *arXiv preprint arXiv:2407.08447* (2024).

Edward W. Larsen. 2007. A generalized Boltzmann equation for non-classical particle transport. In *Proceedings of the International Conference on Mathematics and Computations and Supercomputing in Nuclear Applications*.

Rong Liu, Dylan Sun, Meida Chen, Yue Wang, and Andrew Feng. 2025. Deformable beta splatting. In *Proceedings of SIGGRAPH Conference Papers*. 1–11.

Johannes Meng, Marios Papas, Ralf Habel, Carsten Dachsbacher, Steve Marschner, Markus Gross, and Wojciech Jarosz. 2015. Multi-scale modeling and rendering of granular materials. *ACM Trans. Graph.* 34, 4 (2015), 1–13.

Ben Mildenhall, Pratul P Srinivasan, Matthew Tancik, Jonathan T Barron, Ravi Ramamoorthi, and Ren Ng. 2020. Nerf: Representing scenes as neural radiance fields for view synthesis. In *Proceedings of ECCV*.

Nicolas Moenne-Loccoz, Ashkan Mirzaei, Or Perel, Riccardo de Lutio, Janick Martinez Esturo, Gavriel State, Sanja Fidler, Nicholas Sharp, and Zan Gojcic. 2024. 3D Gaussian Ray Tracing: Fast Tracing of Particle Scenes. *ACM Trans. Graph.* (2024).

Jonathan T. Moon, Bruce Walter, and Stephen R. Marschner. 2007. Rendering discrete random media using precomputed scattering solutions. In *Proceedings of EGSR*.

Thomas Porter and Tom Duff. 1984. Compositing digital images. In *Proceedings of SIGGRAPH*. 253–259.

- Shenhan Qian, Tobias Kirschstein, Liam Schoneveld, Davide Davoli, Simon Giebenhain, and Matthias Nießner. 2024. Gaussianavatars: Photorealistic head avatars with rigged 3D Gaussians. In *Proceedings of CVPR. 20299–20309*.
- Kerui Ren, Lihan Jiang, Tao Lu, Mulin Yu, Linning Xu, Zhangkai Ni, and Bo Dai. 2025. Octree-GS: Towards Consistent Real-time Rendering with LOD-Structured 3D Gaussians. *IEEE Transactions on Pattern Analysis & Machine Intelligence* 01 (2025), 1–15.
- Samuel Rota Bulò, Lorenzo Porzi, and Peter Kotschieder. 2024. Revising densification in Gaussian splatting. In *Proceedings of ECCV*. Springer, 347–362.
- S. Sabour, L. Goli, G. Kopanas, M. Matthews, D. Lagun, L. Guibas, A. Jacobson, D. Fleet, and A. Tagliasacchi. 2025. SpotlessSplats: Ignoring Distractors in 3D Gaussian Splatting. *ACM Trans. Graph.* 44, 2 (2025), 1–11.
- Shunsuke Saito, Gabriel Schwartz, Tomas Simon, Junxuan Li, and Giljoo Nam. 2024. Relightable Gaussian codec avatars. In *Proceedings of CVPR*. 130–141.
- Johannes Lutz Schönberger and Jan-Michael Frahm. 2016. Structure-from-Motion Revisited. In *Proceedings of CVPR*.
- Alvy Ray Smith. 1995. *Alpha and the History of Digital Compositing*. Technical Report. Microsoft Corporation. <https://www.cs.princeton.edu/courses/archive/spr05/cos426/papers/smith95c.pdf>
- Jiaxiang Tang, Jiawei Ren, Hang Zhou, Ziwei Liu, and Gang Zeng. 2024. DreamGaussian: Generative Gaussian splatting for efficient 3D content creation. In *Proceedings of ICLR*.
- Delio Vicini, Wenzel Jakob, and Anton Kaplanyan. 2021a. A non-exponential transmittance model for volumetric scene representations. *ACM Trans. Graph.* 40, 4 (2021), 1–16.
- Delio Vicini, Sébastien Speierer, and Wenzel Jakob. 2021b. Path replay backpropagation: Differentiating light paths using constant memory and linear time. *ACM Trans. Graph.* 40, 4 (2021), 1–14.
- Eugen von Lommel. 1889. Die Photometrie der diffusen Zurückwerfung. (1889).
- Nicolas von Lützwow and Matthias Nießner. 2025. LinPrim: Linear Primitives for Differentiable Volumetric Rendering. *arXiv preprint arXiv:2501.16312* (2025).
- Philip Willis. 2006. Projective Alpha Colour. *Computer Graphics Forum* 25, 1 (2006), 39–54. doi:10.1111/j.1467-8659.2006.00975.x
- Magnus Wrenninge, Ryusuke Villemin, and Christophe Hery. 2017. *Path traced sub-surface scattering using anisotropic phase functions and non-exponential free flights*. Technical Report 17-07. Technical report.
- G. Wu, T. Yi, J. Fang, L. Xie, X. Zhang, W. Wei, W. Liu, Q. Tian, and X. Wang. 2024. 4D Gaussian Splatting for Real-Time Dynamic Scene Rendering. In *Proceedings of CVPR*. 20310–20320.
- Tian-Xing Xu, Wenbo Hu, Yu-Kun Lai, Ying Shan, and Song-Hai Zhang. 2024. Texture-gs: Disentangling the Geometry and Texture for 3D Gaussian Splatting Editing. In *Proceedings of ECCV*. Springer Nature Switzerland, Cham, 37–53.
- Zeyu Yang, Hongye Yang, Zijie Pan, and Li Zhang. 2023. Real-time Photorealistic Dynamic Scene Representation and Rendering with 4D Gaussian Splatting. *arXiv preprint arXiv:2310.10642* (2023).
- Daheng Yin, Isaac Ding, Yili Jin, Jianxin Shi, and Jiangchuan Liu. 2025. TrackerSplat: Exploiting Point Tracking for Fast and Robust Dynamic 3D Gaussians Reconstruction. In *Proceedings of SIGGRAPH Asia 2025 Conference Papers*. 1–11.
- Hongyu Zhou, Jiahao Shao, Lu Xu, Dongfeng Bai, Weichao Qiu, Bingbing Liu, Yue Wang, Andreas Geiger, and Yiyi Liao. 2024a. Hugs: Holistic urban 3D scene understanding via Gaussian splatting. In *Proceedings of CVPR*. 21336–21345.
- Yang Zhou, Songyin Wu, and Ling-Qi Yan. 2024b. Unified Gaussian Primitives for Scene Representation and Rendering. (2024). [arXiv:2406.09733](https://arxiv.org/abs/2406.09733)

A 3D GAUSSIAN SPLATTING AS THE RTE

Here we derive the radiative transfer equation (RTE) for emissive media (Eq. (2)) from the Gaussian splatting image formation model (Eq. (1)). For that, we will start from the inner product term, that accounts for the transparency from previous splats, and define it as the transmittance from \mathbf{x} to the point at splat \mathbf{x}_i as

$$T_i(\mathbf{x}, \mathbf{x}_i) = \prod_{j < i} (1 - \alpha_j(\mathbf{x}_j)). \quad (\text{A.1})$$

Now, using the continuous definition of the medium density in Eq. (3), and by taking M small steps, we can rewrite $T_i(\mathbf{x}, \mathbf{x}_i)$ as

$$T(\mathbf{x}, \mathbf{x}_i) = \prod_{k=0}^M (1 - \sigma(\mathbf{x}_k) \cdot \Delta s), \quad (\text{A.2})$$

with $\mathbf{x}_k = \mathbf{x} + \boldsymbol{\omega} \cdot \Delta s \cdot k$, and $\Delta s = \frac{t_i}{M}$ with $t_i = |\mathbf{x}_i - \mathbf{x}|$. Now, following the derivations from Kostinski [Kostinski 2001], we apply

logarithms to both sides and use a first order approximation on the right to get

$$\begin{aligned} \log(T(\mathbf{x}, \mathbf{x}_i)) &= \log\left(\prod_{k=0}^M \sigma(\mathbf{x}_k) \cdot \Delta s\right) \\ &\approx -\sum_{k=0}^M \sigma(\mathbf{x}_k) \cdot \Delta s, \end{aligned}$$

which by taking the limit $\Delta s \rightarrow 0$, applying exponentials to both sides gives

$$T(\mathbf{x}, \mathbf{x}_i) = \exp\left(-\int_0^{t_i} \sigma(\mathbf{x}_s) ds\right),$$

which is the heterogeneous transmittance predicted by the Beer-Boulder-Lambert law.

Now, using the source and density definitions in Eq. (3), plugging in $T(\mathbf{x}, \mathbf{x}_i)$, and taking M small steps until a maximum distance t_{\max} , we can rewrite Eq. (1) as

$$L_0(\mathbf{x}, \boldsymbol{\omega}) = \sum_{j=0}^M Q(\mathbf{x}_k, \boldsymbol{\omega}) \cdot \sigma(\mathbf{x}_k) \cdot T(\mathbf{x}, \mathbf{x}_k) \cdot \Delta s,$$

which by again taking the limit $\Delta s \rightarrow 0$ and setting $t_{\max} = \infty$ results into the Eq. (2):

$$L_0(\mathbf{x}, \boldsymbol{\omega}) = \int_0^{\infty} Q(\mathbf{x}_k, \boldsymbol{\omega}) \cdot \sigma(\mathbf{x}_k) \cdot T(\mathbf{x}, \mathbf{x}_k) ds. \quad (\text{A.3})$$

B TRANSMITTANCE AS A RUSSIAN-ROULETTE PROCESS

Kheradmand et al. [2025] leveraged stochastic transparency [Enderthon et al. 2010] for avoiding sorting in 3DGS at the cost of introducing variance. For that, they transformed Eq. (1) into a recursive estimator:

$$L_i = E_i \cdot \alpha_i + (1 - \alpha_i) \cdot L_{i+1}, \quad (\text{A.4})$$

which can be solved stochastically via Russian roulette, by choosing whether we draw splat i with probability α_i , or if on the other hand L_{i+1} is drawn. This allows to avoid sorting splats when rasterizing.

This approach is still valid within the framework of the generalized non-exponential light transport: By writing Eq. (A.2) using the differential extinction probability (Eq. (5)) we get

$$T(\mathbf{x}, \mathbf{x}_i) = \prod_{k < 0}^M (1 - \sigma(\mathbf{x}_k, \tau_k) \cdot \Delta s) = \prod_{k < 0}^M \left(1 - \frac{p(\tau_k)}{T(\tau_k)} \cdot \Delta s\right). \quad (\text{A.5})$$

PROOF. Starting with Eq. (A.5) and applying logarithms in both sides, using a first-order approximation of the logarithm, we get

$$\begin{aligned} \log(T(\mathbf{x}, \mathbf{x}_i)) &= \log\left(\prod_{k < 0}^M \left(1 - \frac{p(\tau_k)}{T(\tau_k)} \cdot \Delta s\right)\right) \\ &= \sum_{k < 0}^M \left(\log\left(1 - \frac{p(\tau_k)}{T(\tau_k)} \cdot \Delta s\right)\right) \\ &\approx \sum_{k < 0}^M \left(-\frac{p(\tau_k)}{T(\tau_k)} \cdot \Delta s\right). \end{aligned}$$

Finally, taking the limit $\Delta s \rightarrow 0$, and using the relationship between $p(\tau)$ and $T(\tau)$ (Eq. (5)), and integrating we get

$$\begin{aligned} \log(T(\mathbf{x}, \mathbf{x}_i)) &= \int_0^{t_i} -\frac{p(\tau_s)}{T(\tau_s)} ds \\ &= \int_0^{t_i} -\frac{d}{ds} \frac{T(\tau_s)}{T(\tau_s)} ds \\ &= \log(T(\mathbf{x}, \mathbf{x}_i)). \end{aligned}$$

□

Now, to build the recursive form of our generalized 3DGS from the transmittance defined in Eq. (A.5), we discretize the medium in individual splats, which gives us

$$L_i = E_i \cdot \frac{\bar{p}_i}{T_i} + \left(1 - \frac{\bar{p}_i}{T_i}\right) \cdot L_{i+1}. \quad (\text{A.6})$$

Unfortunately, except for the case of exponential transmittance where $\frac{\bar{p}_i}{T_i} = \alpha_i$, the differential extinction probability defined by $\frac{\bar{p}_i}{T_i}$ is a function of the traversed optical depth (i.e., of all previous splats). Thus, while stochastically we can early terminate the recursion, sorting and evaluating the previous splats is still required.

C ADJOINTS

In order to use path-replay backpropagation for efficient front-to-back differentiable rendering, we cannot completely rely on automatic differentiation for computing the adjoint phase recursively. Here we derive the adjoints for both the linear and quadratic image formation models. Note that the former is a special case of the quadratic transmittance: We include it explicitly since given its simpler form it allows for a more efficient implementation.

In order to compute the adjoints, we will first plug Eq. (8) in Eq. (7), and rewrite L_0 as

$$\begin{aligned} L_0 &= \sum_{i < k} E_i \cdot p_i + E_k \cdot \left(1 - \sum_{i < k} p_i\right) + L_b \cdot \left(1 - \sum_{i=1}^N p_i\right) \\ &= \sum_{i < k} (E_i - E_k - L_b) \cdot p_i + E_k + L_b. \end{aligned}$$

Note that for the background contribution L_b to be visible, transmittance cannot saturate so in practice we can assume that when $k = N$, then $E_k = L_b$, and we can remove L_b from L_0 , leaving

$$\begin{aligned} L_0 &= \sum_{i < k} (E_i - E_k) \cdot p_i + E_k \\ &= \sum_{i < k} \Delta E_i \cdot p_i + E_k. \end{aligned} \quad (\text{A.7})$$

C.1 Linear transmittance

Plugging the $p_{i < k}$ term for linear transmittance into Eq. (A.7) we get

$$L_0 = \sum_{i < k} \Delta E_i \cdot p_i + E_k, \quad (\text{A.8})$$

with derivative

$$\begin{aligned} \delta L_0 &= \sum_{i < k} \delta (\Delta E_i \cdot \alpha_i) + \delta E_k \\ &= \sum_{i < k} (\delta E_i \cdot \alpha_i + E_i \cdot \delta \alpha_i - \delta E_k \cdot \alpha_i - E_k \cdot \delta \alpha_i) + \delta E_k \\ &= \sum_{i < k} \left(\delta (E_i \cdot \alpha_i) - E_k \cdot \delta \alpha_i \right) + \delta E_k \cdot \left(1 - \sum_{i < k} \alpha_i\right), \end{aligned}$$

which can be written recursively as

$$\delta L_i = \begin{cases} \left(\delta (E_i \cdot \alpha_i) - E_k \cdot \delta \alpha_i \right) + \delta L_{i+1} & i < k \\ \delta E_k \cdot \bar{T}_k & i = k \\ 0 & \text{otherwise,} \end{cases} \quad (\text{A.9})$$

where \bar{T}_k can be computed from previous iterations, and E_k needs to be computed in the forward pass and passed as input to the adjoint pass.

C.2 Quadratic transmittance

Plugging the $p_{i < k}$ term for quadratic transmittance into Eq. (A.7) we get

$$\begin{aligned} L_0 &= \sum_{i < k} \Delta E_i \cdot \alpha_i \cdot \left(1 + c \cdot \sum_{j < i} \alpha_j\right) + E_k \\ &= \sum_{i < k} \Delta E_i \cdot \alpha_i + c \cdot \sum_{i < k} \left(\Delta E_i \cdot \alpha_i \cdot \sum_{j < i} \alpha_j \right) + E_k. \end{aligned} \quad (\text{A.10})$$

The second sum can be expanded as

$$\begin{aligned} \sum_{i=0}^N \Delta E_i \cdot \alpha_i \cdot \sum_{j=0}^{i-1} \alpha_j &= 0 \cdot \Delta E_0 \cdot \alpha_0 + \alpha_0 \cdot \Delta E_1 \cdot \alpha_1 \\ &+ (\alpha_0 + \alpha_1) \cdot \Delta E_2 \cdot \alpha_2 + \dots \\ &= \alpha_0 \cdot (\Delta E_1 \cdot \alpha_1 + \Delta E_2 \cdot \alpha_2 + \dots) \\ &+ \alpha_1 \cdot (\Delta E_2 \cdot \alpha_2 + \Delta E_3 \cdot \alpha_3 + \dots) + \dots \\ &= \sum_{i=0}^N \left(\alpha_i \cdot \sum_{j=i+1}^N \Delta E_j \cdot \alpha_j \right). \end{aligned}$$

Now taking the derivative using the produce rule, and using the definition of the discrete optical depth $\bar{\tau}_i = \sum_{j<i} \alpha_j$ we get

$$\begin{aligned}
\delta L_0 &= \sum_{i<k} \delta(\Delta E_i \cdot \alpha_i) + c \cdot \sum_{i<k} \left(\delta(\Delta E_i \cdot \alpha_i) \cdot \sum_{j=0}^{i-1} \alpha_j \right) \\
&\quad + c \cdot \sum_{i<k} \left(\Delta E_i \cdot \alpha_i \cdot \sum_{j=0}^{i-1} \delta \alpha_j \right) + \delta E_k \\
&= \sum_{i<k} \delta(\Delta E_i \cdot \alpha_i) + c \cdot \sum_{i<k} \left(\delta(\Delta E_i \cdot \alpha_i) \cdot \sum_{j=0}^{i-1} \alpha_j \right) \\
&\quad + c \cdot \sum_{i<k} \left(\delta \alpha_i \cdot \sum_{j=i+1}^{k-1} \Delta E_j \cdot \alpha_j \right) + \delta E_k \\
&= \sum_{i<k} (\delta(\Delta E_i \cdot \alpha_i) + c \cdot \delta(\Delta E_i \cdot \alpha_i) \cdot \bar{\tau}_i \\
&\quad + c \cdot \delta \alpha_i \cdot \sum_{j=i+1}^{k-1} \Delta E_j \cdot \alpha_j) + \delta E_k \\
&= \sum_{i<k} \left(\delta(\Delta E_i \cdot \alpha_i) \cdot (1 + c \cdot \bar{\tau}_i) + c \cdot \delta \alpha_i \cdot \Theta_i \right) + \delta E_k,
\end{aligned}$$

with Θ_i defined recursively as

$$\Theta_i = \begin{cases} \sum_{j=1}^{k-1} \Delta E_j \cdot \alpha_j & i = 0 \\ \Theta_{i-1} - \Delta E_i \cdot \alpha_i & i > 0. \end{cases}$$

Further expanding ΔE_i in δL_0 we get

$$\begin{aligned}
\delta L_0 &= \sum_{i<k} \left((\delta(E_i \cdot \alpha_i) - \delta E_k \cdot \alpha_i - E_k \cdot \delta \alpha_i) \cdot (1 + c \cdot \bar{\tau}_i) \right. \\
&\quad \left. + c \cdot \delta \alpha_i \cdot \Theta_i \right) + \delta E_k \\
&= \sum_{i<k} \left((\delta(E_i \cdot \alpha_i) - E_k \cdot \delta \alpha_i) \cdot (1 + c \cdot \bar{\tau}_i) - \delta E_k \cdot \alpha_i \cdot (1 + c \cdot \bar{\tau}_i) \right. \\
&\quad \left. + c \cdot \delta \alpha_i \cdot \Theta_i \right) + \delta E_k \\
&= \sum_{i<k} \left((\delta(E_i \cdot \alpha_i) - E_k \cdot \delta \alpha_i) \cdot (1 + c \cdot \bar{\tau}_i) + c \cdot \delta \alpha_i \cdot \Theta_i \right) \\
&\quad + \delta E_k \cdot \left(1 - \sum_{i<k} \alpha_i \cdot (1 + c \cdot \bar{\tau}_i) \right) \\
&= \sum_{i<k} \left((\delta(E_i \cdot \alpha_i) - E_k \cdot \delta \alpha_i) \cdot (1 + c \cdot \bar{\tau}_i) + c \cdot \delta \alpha_i \cdot \Theta_i \right) + \delta E_k \cdot p_k.
\end{aligned}$$

With this, we can obtain a recursive formula for the adjoint:

$$\delta L_i = \begin{cases} (\delta(E_i \cdot \alpha_i) - E_k \cdot \delta \alpha_i) \cdot (1 + c \cdot \bar{\tau}_i) + c \cdot \delta \alpha_i \cdot \Theta_i + \delta L_{i+1} & i < k \\ \delta E_k \cdot \bar{T}_k & i = k \\ 0 & \text{otherwise.} \end{cases} \quad (\text{A.11})$$

Both $\bar{\tau}_i$ and \bar{T}_k can be computed recursively from previous iterations in the backward pass, while Θ_i requires Θ_0 , which can be precomputed in the forward pass, and passed as input to the adjoint pass with E_k .